Available online at www.sciencedirect.com
SCIENCE DIRECT®
Journal of Computational Physics 191 (2003) 206–227
JOURNAL OF COMPUTATIONAL PHYSICS
www.elsevier.com/locate/jcp

Design and analysis of ALE schemes with provable second-order time-accuracy for inviscid and viscous flow simulations

Philippe Geuzaine [a,*], Céline Grandmont [b], Charbel Farhat [a]

[a] *Department of Aerospace Engineering Sciences and Center for Aerospace Structures, University of Colorado at Boulder, Boulder, CO 80309-0429, USA*
[b] *CEREMADE, Université Paris Dauphine, 75775 Paris Cedex 16, France*

Received 25 November 2002; received in revised form 4 June 2003; accepted 4 June 2003

Abstract

We consider the solution of inviscid as well as viscous unsteady flow problems with moving boundaries by the arbitrary Lagrangian–Eulerian (ALE) method. We present two computational approaches for achieving formal second-order time-accuracy on moving grids. The first approach is based on flux time-averaging, and the second one on mesh configuration time-averaging. In both cases, we prove that formally second-order time-accurate ALE schemes can be designed. We illustrate our theoretical findings and highlight their impact on practice with the solution of inviscid as well as viscous, unsteady, nonlinear flow problems associated with the AGARD Wing 445.6 and a complete F-16 configuration.

Keywords: ALE; Moving grids; Second-order time-accuracy; Geometric conservation law; Aeroelasticity

1. Introduction

In many computational fluid dynamics (CFD) applications, some or all of the boundaries delimiting the physical domain of the flow move in time. Examples include, among others, a large class of free-surface flow problems and a wide variety of fluid–structure interaction problems. When the moving boundaries undergo large displacements and/or rotations, or when they experience large deformations, the flow problem is often formulated in an arbitrary Lagrangian–Eulerian (ALE) [1,2] frame and discretized on an unstructured moving grid. Such a discretization differs from that of the standard Eulerian formulation only in the introduction of some geometric quantities involving the positions and velocities of the moving grid points. For this reason, an ALE time-integrator is typically constructed by combining a preferred time-

* Corresponding author. Present address: Avenue Jean Mermoz 30, 6041 Gosselies, Belgium. Tel.: +32-71-919334; fax: +32-71-919331.
E-mail address: philippe.geuzaine@cenaero.be (P. Geuzaine).

0021-9991/$ - see front matter
doi:10.1016/S0021-9991(03)00311-5

integrator for fixed grids computations and an ad hoc procedure for evaluating the geometric quantities arising from the ALE formulation. As noted in [3,4], such an approach for designing an ALE time-integrator does not necessarily preserve the order of time-accuracy of its fixed grid counterpart. To address this issue, we present two different methods for extending to moving grids a preferred time-integrator while preserving its order of time-accuracy established on fixed grids. These methods differ in the approaches they adopt for time-integrating between time t^n and time t^{n+1} the convective, diffusive and source terms, when the grid moves from a position x^n to a position x^{n+1} (here and in the remainder of this paper, the superscript n designates the nth time-instance t^n). For each time-interval $[t^n, t^{n+1}]$, the first method constructs a set of intermediate mesh configurations, evaluates the numerical fluxes and source terms on each one of them, then time-averages each set of these numerical quantities. Alternatively, the second method defines a unique computational mesh configuration in the time-interval $[t^n, t^{n+1}]$ by time-averaging the intermediate mesh configurations themselves, then computes the numerical fluxes and source terms on this time-averaged mesh configuration. In both methods, the geometric quantities arising from the ALE formulation, the parameters governing the construction of the intermediate mesh configurations and the time-averaging procedure are chosen as to guarantee that the resulting ALE time-integrator is formally p-order time-accurate on moving grids, where p characterizes the underlying fixed grid time-integrator.

It turns out that for a given fixed grid time-integrator, each of the methods outlined above leads to multiple ALE versions which preserve its order of time-accuracy on moving grids. However, it is interesting to note that not all of these versions satisfy their discrete geometric conservation laws (DGCL). A DGCL [5,6] states that the computation of the geometric parameters arising from an ALE formulation must be performed in such a way that, independently of the mesh motion, the ALE numerical scheme preserves the state of a uniform flow. Therefore, whereas in [6] the authors proved that satisfying the DGCL is a sufficient condition for an ALE numerical scheme to be consistent on moving grids, and in [7,8] the authors proved that this law is a necessary and sufficient condition for some ALE numerical schemes to preserve on moving grids the nonlinear stability of their fixed grid counterparts, in this paper we show that the DGCL is neither a necessary nor a sufficient condition for an ALE numerical scheme to preserve on moving grids its order of time-accuracy established on fixed grids. Hence, an additional contribution of this paper is a further characterization of the DGCL.

We organize the remainder of this paper as follows. In Section 2, we overview the ALE formulation of the Navier–Stokes equations and specify the semi-discretization method adopted in this work. In Section 3, we expose the two approaches outlined above for extending to moving grids a time-integrator developed for fixed grids, while preserving its order of time-accuracy established on fixed meshes. We perform in Section 4 the accuracy analysis of both approaches for the case of the popular three-point backward difference scheme. This error analysis, which is based on the investigation of the local truncation error as in [3], leads to a couple of ALE extensions of this scheme that are presented and contrasted with simpler ones in Section 5. In Section 6, we illustrate our theoretical findings and highlight their impact on practice with the solution of inviscid as well as viscous, unsteady, nonlinear flow problems associated with the AGARD Wing 445.6 and an F-16 fighter. We conclude this paper in Section 7.

2. ALE method for the solution of flow problems on moving grids

2.1. ALE formulation of the Navier–Stokes equations

Let $\Omega(x,t) \subset \mathbb{R}^3 \times [0,\infty[$ be the instantaneous configuration where the coordinates of a point in space are denoted by $x = (x_j)_{j\in\{1,2,3\}}$ and time is denoted by t, and let $\Omega(\xi,0)$ be the reference configuration where the coordinates of a point in space are denoted by $\xi = (\xi_j)_{j\in\{1,2,3\}}$ and time is denoted by τ. We define a mapping function between $\Omega(x,t)$ and $\Omega(\xi,0)$ as follows:

$$x = x(\xi, \tau), \quad t = \tau, \tag{1}$$

and denote by J its determinant

$$J = \det\left(\frac{\partial x}{\partial \xi}\right). \tag{2}$$

The ALE conservative form of the Navier–Stokes equations (possibly supplemented by a turbulence model) can be written as

$$\left.\frac{\partial Ju}{\partial t}\right|_{\xi} + J\nabla_x \cdot (F(u) - wu) = J\nabla_x \cdot R(u) + JS(u), \tag{3}$$

where

$$w = \left.\frac{\partial x}{\partial t}\right|_{\xi}, \tag{4}$$

u denotes the conservative fluid state vector, F and R represent, respectively, the convective and diffusive fluxes, and S denotes the source term associated with a turbulence model.

2.2. Semi-discretization

In this work, we consider the case where Eq. (3) is semi-discretized by a combination of the finite volume method for the convective term, and the finite element method for the diffusive and source terms. In this case, the resulting semi-discrete equations can be written as

$$\frac{\mathrm{d}}{\mathrm{d}t}(\Omega_i u_i) + f_i(u, x, w) = g_i(u, x), \tag{5}$$

where Ω_i denotes the control volume of the ith cell associated with a given mesh, u_i denotes the average value of the fluid state vector over this cell, x and w are the vectors collecting the time-dependent values of grid point positions and velocities, respectively, f_i denotes the numerical convective flux, and g_i represents the numerical diffusive and source terms. We emphasize that here and throughout the remainder of this paper, u, x and w represent discrete rather than continuous values. We note that a pure finite volume or a pure (stabilized) finite element method leads to similar semi-discrete equations. We also note that when a finite volume method is used to discretize the convective fluxes, Eq. (5) can be rewritten as

$$\frac{\mathrm{d}}{\mathrm{d}t}(\Omega_i u_i) + f_i(u, v, \kappa) = g_i(u, x), \tag{6}$$

where v and $\kappa = w \cdot v$ are, respectively, the vectors storing the discrete values of the normal and normal velocity at the interfaces of the control volumes, and for simplicity the same notation for the numerical convective flux is used. In general, the normal v is a nonlinear function φ of the discrete mesh position vector

$$v = \varphi(x). \tag{7}$$

3. Design of ALE time-integrators

In this paper, we focus on the extension to moving grids of the popular *second-order* time-accurate three-point backward difference scheme. However, we note that the issues we raise, the methodologies we present, and the solutions we propose equally apply to other fixed-grid time-integrators.

The time-integration between t^n and t^{n+1} of the semi-discrete equations (5) or (6) raises the issue of where to evaluate the terms f_i and g_i: on the mesh configuration x^n at t^n, or on x^{n+1} at t^{n+1}, or in between these two configurations, or outside these two configurations, or using a combination of all these mesh configurations? We consider two approaches for addressing this issue, both of which begin with identifying and evaluating two different sequences of mesh configurations: one sequence with K_f configurations for time-integrating the convective fluxes, and one sequence with K_g configurations for time-integrating the diffusive fluxes and source terms [9,10].

In the first approach, we evaluate the numerical convective, diffusive and source terms on each identified mesh configuration, then time-average their values. Hence, assuming for simplicity but without any loss of generality a constant time-step Δt, this approach applied to the three-point backward difference scheme discretizes Eq. (5) into

$$\frac{3}{2}(\Omega u)_i^{n+1} - 2(\Omega u)_i^n + \frac{1}{2}(\Omega u)_i^{n-1} + \Delta t \sum_{k=1}^{K_f} \alpha_k f_i(u^{n+1}, x_f^{(k)}, w^{(k)}) = \Delta t \sum_{k=1}^{K_g} \beta_k g_i(u^{n+1}, x_g^{(k)}), \tag{8}$$

where the kth mesh position $x_f^{(k)}$, its corresponding velocity field $w^{(k)}$, and the coefficients α_k are associated with the time-averaging of the convective fluxes, and the kth mesh position $x_g^{(k)}$ and the coefficients β_k are associated with the time-averaging of the diffusive and source terms.

In the second approach, we time-average each sequence of mesh configurations, then compute for each time-averaged mesh configuration the corresponding convective flux or combined diffusive and source terms. When applied to Eq. (6), this approach gives

$$\frac{3}{2}(\Omega u)_i^{n+1} - 2(\Omega u)_i^n + \frac{1}{2}(\Omega u)_i^{n-1} + \Delta t\, f_i(u^{n+1}, \bar{v}, \bar{\kappa}) = \Delta t\, g_i(u^{n+1}, \bar{x}), \tag{9}$$

where

$$\bar{v} = \sum_{k=1}^{K_f} \alpha_k \varphi(x_f^{(k)}), \tag{10a}$$

$$\bar{\kappa} = \sum_{k=1}^{K_f} \alpha_k w^{(k)} \cdot \varphi(x_f^{(k)}), \tag{10b}$$

$$\bar{x} = \sum_{k=1}^{K_g} \beta_k x_g^{(k)}. \tag{10c}$$

In principle, each of the approaches described above for designing an ALE time-integrator applies to both forms (5) and (6) of the semi-discrete ALE form of the Navier–Stokes equations. However, to be concise, we consider in this paper the application of the first approach to form (5) and that of the second approach to form (6). In general, the two time-averaging approaches outlined previously lead to different numerical ALE schemes because the terms f_i and g_i are nonlinear functions of the mesh position. The first approach is more flexible and more general, but the second approach is computationally more efficient. In both approaches, the mesh configurations and their weighting coefficients are unknowns that we propose to determine by requiring that the resulting numerical scheme preserves the order of time-accuracy of its fixed-grid counterpart. To this effect, we parameterize in both cases each kth mesh position and velocity field as

$$x_f^{(k)} = \zeta_k^{n+1} x^{n+1} + \zeta_k^n x^n + \zeta_k^{n-1} x^{n-1}, \tag{11a}$$

$$w^{(k)} = \frac{\theta_k^{n+1} x^{n+1} + \theta_k^n x^n + \theta_k^{n-1} x^{n-1}}{\Delta t}, \tag{11b}$$

$$x_g^{(k)} = \eta_k^{n+1} x^{n+1} + \eta_k^n x^n + \eta_k^{n-1} x^{n-1}. \tag{11c}$$

The coefficients ζ, θ, and η are so far unspecified. We note that the restriction of the above parameterization to the mesh configurations at t^{n-1}, t^n, and t^{n+1} is due to our focus on the three-point backward difference scheme.

4. Error analysis

We start by considering the first approach in which the fluxes and source terms are time-averaged, and state the following result.

Proposition 1. *If the parameterization* (11a)–(11c) *satisfies*

$$\zeta_k^{n+1} + \zeta_k^n + \zeta_k^{n-1} = 1 \quad \forall k, \tag{12a}$$

$$\theta_k^{n+1} + \theta_k^n + \theta_k^{n-1} = 0 \quad \forall k, \tag{12b}$$

$$\theta_k^n + 2\theta_k^{n-1} = -1 \quad \forall k, \tag{12c}$$

$$\sum_{k=1}^{K_f} \alpha_k = 1, \tag{12d}$$

$$\sum_{k=1}^{K_f} \alpha_k \left[\zeta_k^n + 2\zeta_k^{n-1}\right] = 0, \tag{12e}$$

$$\sum_{k=1}^{K_f} \alpha_k \left[\theta_k^n + 4\theta_k^{n-1}\right] = 0, \tag{12f}$$

$$\eta_k^{n+1} + \eta_k^n + \eta_k^{n-1} = 1 \quad \forall k, \tag{12g}$$

$$\sum_{k=1}^{K_g} \beta_k = 1, \tag{12h}$$

$$\sum_{k=1}^{K_g} \beta_k \left[\eta_k^n + 2\eta_k^{n-1}\right] = 0 \tag{12i}$$

and the continuous functions $\Omega u, f$, and g are sufficiently smooth, then the ALE version of the three-point backward difference scheme (8) *is second-order time-accurate on moving grids.*

Proof. Let

$$\Psi_i = \frac{3}{2}(\Omega u)_i(t^{n+1}) - 2(\Omega u)_i(t^n) + \frac{1}{2}(\Omega u)_i(t^{n-1}) + \Delta t \sum_{k=1}^{K_f} \alpha_k f_i(u(t^{n+1}), x_f(t^{(k)}), w(t^{(k)})) - \Delta t \sum_{k=1}^{K_g} \beta_k g_i(u(t^{n+1}), x_g(t^{(k)})) \tag{13}$$

denote the local truncation error where

$$x_f(t^{(k)}) = \zeta_k^{n+1} x(t^{n+1}) + \zeta_k^n x(t^n) + \zeta_k^{n-1} x(t^{n-1}), \tag{14a}$$

$$w(t^{(k)}) = \frac{\theta_k^{n+1} x(t^{n+1}) + \theta_k^n x(t^n) + \theta_k^{n-1} x(t^{n-1})}{\Delta t}, \tag{14b}$$

$$x_g(t^{(k)}) = \eta_k^{n+1} x(t^{n+1}) + \eta_k^n x(t^n) + \eta_k^{n-1} x(t^{n-1}). \tag{14c}$$

with $t^{(k)}$ denoting the fictitious time associated with the kth mesh configuration. If the continuous function Ωu is sufficiently smooth, $(\Omega u)_i$ can be expanded around t^{n+1} as follows:

$$(\Omega u)_i(t^n) = (\Omega u)_i(t^{n+1}) - \Delta t \frac{\mathrm{d}}{\mathrm{d}t}(\Omega u)_i(t^{n+1}) + \frac{\Delta t^2}{2}\frac{\mathrm{d}^2}{\mathrm{d}t^2}(\Omega u)_i(t^{n+1}) + \mathrm{O}(\Delta t^3), \tag{15}$$

$$(\Omega u)_i(t^{n-1}) = (\Omega u)_i(t^{n+1}) - 2\Delta t \frac{\mathrm{d}}{\mathrm{d}t}(\Omega u)_i(t^{n+1}) + 2\Delta t^2 \frac{\mathrm{d}^2}{\mathrm{d}t^2}(\Omega u)_i(t^{n+1}) + \mathrm{O}(\Delta t^3). \tag{16}$$

It follows that

$$\begin{aligned}\frac{3}{2}(\Omega u)_i^{n+1} - 2(\Omega u)_i^n + \frac{1}{2}(\Omega u)_i^{n-1} &= \Delta t \frac{\mathrm{d}}{\mathrm{d}t}(\Omega u)_i(t^{n+1}) + \mathrm{O}(\Delta t^3) \\ &= -\Delta t f_i(u(t^{n+1}), x(t^{n+1}), w(t^{n+1})) + \Delta t g_i(u(t^{n+1}), x(t^{n+1})) + \mathrm{O}(\Delta t^3).\end{aligned} \tag{17}$$

Similarly, if the continuous functions f and g are sufficiently smooth, then

$$\begin{aligned}f_i(u(t^{n+1}), x_f(t^{(k)}), w(t^{(k)})) = {} & f_i(u(t^{n+1}), x(t^{n+1}), w(t^{n+1})) + \nabla_x f_i(u(t^{n+1}), x(t^{n+1}), w(t^{n+1}))(x_f(t^{(k)}) - x(t^{n+1})) \\ & + \nabla_w f_i(u(t^{n+1}), x(t^{n+1}), w(t^{n+1}))(w(t^{(k)}) - w(t^{n+1})) + \mathrm{O}(\|x_f(t^{(k)}) - x(t^{n+1})\|^2 \\ & + \|w(t^{(k)}) - w(t^{n+1})\|^2),\end{aligned} \tag{18}$$

and

$$\begin{aligned}g_i(u(t^{n+1}), x_g(t^{(k)})) = {} & g_i(u(t^{n+1}), x(t^{n+1})) + \nabla_x g_i(u(t^{n+1}), x(t^{n+1}))(x_g(t^{(k)}) - x(t^{n+1})) \\ & + \mathrm{O}(\|x_g(t^{(k)}) - x(t^{n+1})\|^2).\end{aligned} \tag{19}$$

From the above results, it follows that

$$\begin{aligned}\Psi_i = {} & \Delta t\left[\left(\sum_{k=1}^{K_f}\alpha_k\right)-1\right]f_i(u(t^{n+1}),x(t^{n+1}),w(t^{n+1})) \\ & + \Delta t\nabla_x f_i(u(t^{n+1}),x(t^{n+1}),w(t^{n+1}))\left[\sum_{k=1}^{K_f}\alpha_k\left[x_f(t^{(k)})-x(t^{n+1})\right]\right] \\ & + \Delta t\nabla_w f_i(u(t^{n+1}),x(t^{n+1}),w(t^{n+1}))\left[\sum_{k=1}^{K_f}\alpha_k\left[w(t^{(k)})-w(t^{n+1})\right]\right] \\ & - \Delta t\left[\left(\sum_{k=1}^{K_g}\beta_k\right)-1\right]g_i(u(t^{n+1}),x(t^{n+1})) - \Delta t\nabla_x g_i(u(t^{n+1}),x(t^{n+1}))\left[\sum_{k=1}^{K_g}\beta_k\left[x_g(t^{(k)})-x(t^{n+1})\right]\right] \\ & + \Delta t\sum_{k=1}^{K_f}\alpha_k\mathrm{O}(\|x_f(t^{(k)})-x(t^n)\|^2+\|w(t^{(k)})-w(t^n)\|^2) - \Delta t\sum_{k=1}^{K_g}\beta_k\mathrm{O}(\|x_g(t^{(k)})-x(t^n)\|^2)+\mathrm{O}(\Delta t^3).\end{aligned} \tag{20}$$

Now, expanding the parameterization (14a)–(14c) into Taylor series as follows:

$$x_f(t^{(k)})-x(t^{n+1}) = (\zeta_k^{n+1}+\zeta_k^n+\zeta_k^{n-1}-1)x(t^{n+1}) - \Delta t(\zeta_k^n+2\zeta_k^{n-1})\dot{x}(t^{n+1})+\mathrm{O}(\Delta t^2), \tag{21}$$

$$\begin{aligned}w(t^{(k)})-w(t^{n+1}) = {} & \frac{1}{\Delta t}(\theta_k^{n+1}+\theta_k^n+\theta_k^{n-1})x(t^{n+1}) - (\theta_k^n+2\theta_k^{n-1}+1)w(t^{n+1}) \\ & + \frac{\Delta t}{2}(\theta_k^n+4\theta_k^{n-1})\dot{w}(t^{n+1})+\mathrm{O}(\Delta t^2),\end{aligned} \tag{22}$$

and

$$x_g(t^{(k)})-x(t^{n+1}) = (\eta_k^{n+1}+\eta_k^n+\eta_k^{n-1}-1)x(t^{n+1}) - \Delta t(\eta_k^n+2\eta_k^{n-1})\dot{x}(t^{n+1})+\mathrm{O}(\Delta t^2), \tag{23}$$

where a dot designates a time-derivative and $w(t^{n+1})=\dot{x}(t^{n+1})$. Choosing the parameters ζ, θ and η as to satisfy the conditions (12a)–(12c) and (12g) makes all the quantities $x_f(t^{(k)})-x(t^n)$, $w(t^{(k)})-w(t^n)$ and $x_g(t^{(k)})-x(t^n)$ become $\mathrm{O}(\Delta t)$. Consequently, the local truncation error becomes

$$\begin{aligned}\Psi_i = {} & \Delta t\left[\left(\sum_{k=1}^{K_f}\alpha_k\right)-1\right]f_i(u(t^{n+1}),x(t^{n+1}),w(t^{n+1})) \\ & + \Delta t^2\left[\sum_{k=1}^{K_f}\alpha_k\left[\zeta_k^n+2\zeta_k^{n-1}\right]\right]\nabla_x f_i(u(t^{n+1}),x(t^{n+1}),w(t^{n+1}))\dot{x}(t^{n+1}) \\ & + \frac{\Delta t^2}{2}\left[\sum_{k=1}^{K_f}\alpha_k\left[\theta_k^n+4\theta_k^{n-1}\right]\right]\nabla_w f_i(u(t^{n+1}),x(t^{n+1}),w(t^{n+1}))\dot{w}(t^{n+1}) \\ & - \Delta t\left[\left(\sum_{k=1}^{K_g}\beta_k\right)-1\right]g_i(u(t^{n+1}),x(t^{n+1})) \\ & - \Delta t^2\left[\sum_{k=1}^{K_g}\beta_k\left[\eta_k^n+2\eta_k^{n-1}\right]\right]\nabla_x g_i(u(t^{n+1}),x(t^{n+1}))\dot{x}(t^{n+1})+\mathrm{O}(\Delta t^3).\end{aligned} \tag{24}$$

Hence, from Eq. (24), it follows that if the conditions (12d)–(12f), (12h) and (12i) are also satisfied, $\Psi_i = \mathrm{O}(\Delta t^3)$ and therefore the extension to moving grids of the three-point backward difference scheme is second-order time-accurate on moving grids. □

Next, we consider the second approach in which the mesh configurations themselves are time-averaged, and state the following result.

Proposition 2. *If the parameterization* (11a)–(11c) *satisfies*

$$\zeta_k^{n+1} + \zeta_k^n + \zeta_k^{n-1} = 1 \quad \forall k, \tag{25a}$$

$$\sum_{k=1}^{K_f} \alpha_k \left[\theta_k^{n+1} + \theta_k^n + \theta_k^{n-1}\right] = 0, \tag{25b}$$

$$\sum_{k=1}^{K_f} \alpha_k \left[\theta_k^n + 2\theta_k^{n-1}\right] = -1, \tag{25c}$$

$$\sum_{k=1}^{K_f} \alpha_k = 1, \tag{25d}$$

$$\sum_{k=1}^{K_f} \alpha_k \left[\zeta_k^n + 2\zeta_k^{n-1}\right] = 0, \tag{25e}$$

$$\sum_{k=1}^{K_f} \alpha_k \left[\theta_k^n + 4\theta_k^{n-1}\right] = 0, \tag{25f}$$

$$\sum_{k=1}^{K_g} \beta_k \left[\eta_k^{n+1} + \eta_k^n + \eta_k^{n-1}\right] = 1, \tag{25g}$$

$$\sum_{k=1}^{K_g} \beta_k = 1, \tag{25h}$$

$$\sum_{k=1}^{K_g} \beta_k \left[\eta_k^n + 2\eta_k^{n-1}\right] = 0 \tag{25i}$$

and the continuous functions $\Omega u, f$, and g are sufficiently smooth, then the ALE version of the three-point backward difference scheme (9) *is second-order time-accurate on moving grids.*

Proof. The local truncation error of the ALE scheme (9) is

$$\Psi_i = \frac{3}{2}(\Omega u)_i(t^{n+1}) - 2(\Omega u)_i(t^n) + \frac{1}{2}(\Omega u)_i(t^{n-1}) + \Delta t f_i(u(t^{n+1}), \bar{v}(t^{n+1}), \bar{\kappa}(t^{n+1})) - \Delta t g_i(u(t^{n+1}), \bar{x}(t^{n+1})), \tag{26}$$

where

$$\bar{v}(t^{n+1}) = \sum_{k=1}^{K_f} \alpha_k \varphi(x_f(t^{(k)})), \tag{27a}$$

$$\bar{\kappa}(t^{n+1}) = \sum_{k=1}^{K_f} \alpha_k w(t^{(k)}) \cdot \varphi(x(t^{(k)})), \tag{27b}$$

$$\bar{x}(t^{n+1}) = \sum_{k=1}^{K_g} \beta_k x_g(t^{(k)}). \tag{27c}$$

From the Taylor series

$$\begin{aligned} f_i(u(t^{n+1}), \bar{v}(t^{n+1}), \bar{\kappa}(t^{n+1})) = {} & f_i(u(t^{n+1}), v(t^{n+1}), \kappa(t^{n+1})) + \nabla_v f_i(u(t^{n+1}), v(t^{n+1}), \kappa(t^{n+1}))(\bar{v}(t^{n+1}) - v(t^{n+1})) \\ & + \nabla_\kappa f_i(u(t^{n+1}), v(t^{n+1}), \kappa(t^{n+1}))(\bar{\kappa}(t^{n+1}) - \kappa(t^{n+1})) \\ & + \mathrm{O}(\|\bar{v}(t^{n+1}) - v(t^{n+1})\|^2 + \|\bar{\kappa}(t^{n+1}) - \kappa(t^{n+1})\|^2), \end{aligned} \tag{28}$$

$$\begin{aligned} g_i(u(t^{n+1}), \bar{x}(t^{n+1})) = {} & g_i(u(t^{n+1}), x(t^{n+1})) + \nabla_x g_i(u(t^{n+1}), x(t^{n+1}))(\bar{x}(t^{n+1}) - x(t^{n+1})) \\ & + \mathrm{O}(\|\bar{x}(t^{n+1}) - x(t^{n+1})\|^2), \end{aligned} \tag{29}$$

and

$$\frac{3}{2}(\Omega u)_i^{n+1} - 2(\Omega u)_i^n + \frac{1}{2}(\Omega u)_i^{n-1} = -\Delta t f_i(u(t^{n+1}), v(t^{n+1}), \kappa(t^{n+1})) + \Delta t g_i(u(t^{n+1}), x(t^{n+1})) + \mathrm{O}(\Delta t^3), \tag{30}$$

Ψ_i can be rewritten as

$$\begin{aligned} \Psi_i = {} & \Delta t \nabla_v f_i(u(t^{n+1}), v(t^{n+1}), \kappa(t^{n+1}))(\bar{v}(t^{n+1}) - v(t^{n+1})) + \Delta t \nabla_\kappa f_i(u(t^{n+1}), v(t^{n+1}), \kappa(t^{n+1}))(\bar{\kappa}(t^{n+1}) - \kappa(t^{n+1})) \\ & - \Delta t \nabla_x g_i(u(t^{n+1}), x(t^{n+1}))(\bar{x}(t^{n+1}) - x(t^{n+1})) + \Delta t \mathrm{O}(\|\bar{v}(t^{n+1}) - v(t^{n+1})\|^2 + \|\bar{\kappa}(t^{n+1}) - \kappa(t^{n+1})\|^2) \\ & - \Delta t \mathrm{O}(\|\bar{x}(t^{n+1}) - x(t^{n+1})\|^2) + \mathrm{O}(\Delta t^3). \end{aligned} \tag{31}$$

If condition (25d) is satisfied, then

$$\begin{aligned} \bar{v}(t^{n+1}) - v(t^{n+1}) &= \sum_{k=1}^{K_f} \alpha_k \big(\varphi(x_f(t^{(k)})) - \varphi(x(t^{n+1}))\big) \\ &= \sum_{k=1}^{K_f} \alpha_k \Big(\nabla_x \varphi(x(t^{n+1}))(x_f(t^{(k)}) - x(t^{n+1})) + \mathrm{O}(\|x_f(t^{(k)}) - x(t^{n+1})\|^2)\Big), \end{aligned} \tag{32}$$

and

$$\begin{aligned} \bar{\kappa}(t^{n+1}) - \kappa(t^{n+1}) &= \sum_{k=1}^{K_f} \alpha_k \big(w(t^{(k)}) \cdot \varphi(x_f(t^{(k)})) - w(t^{n+1}) \cdot \varphi(x(t^{n+1}))\big) \\ &= \sum_{k=1}^{K_f} \alpha_k \big((w(t^{(k)}) - w(t^{n+1})) \cdot \varphi(x_f(t^{(k)}))\big) + w(t^{n+1}) \cdot (\bar{v}(t^{n+1}) - v(t^{n+1})). \end{aligned} \tag{33}$$

Now, performing the Taylor expansion of $\varphi(x_f(t^{(k)}))$ around $\varphi(x(t^{n+1}))$, recalling Eq. (21), and satisfying condition (25a) transforms the above equation into

$$\bar{\kappa}(t^{n+1}) - \kappa(t^{n+1}) = \sum_{k=1}^{K_f} \alpha_k \big((w(t^{(k)}) - w(t^{n+1})) \cdot (\varphi(x(t^{n+1})) + \mathrm{O}(\Delta t)) \big) + w(t^{n+1}) \cdot (\bar{v}(t^{n+1}) - v(t^{n+1})). \tag{34}$$

Finally, if condition (25h) is also satisfied, then

$$\bar{x}(t^{n+1}) - x(t^{n+1}) = \sum_{k=1}^{K_g} \beta_k \big(x_g(t^{(k)}) - x(t^{n+1}) \big). \tag{35}$$

Hence, from Eqs. (32), (34) and (35) and Eqs. (21)–(23), it follows that the quantities $\bar{v}(t^{n+1}) - v(t^{n+1})$, $\bar{\kappa}(t^{n+1}) - \kappa(t^{n+1})$ and $\bar{x}(t^{n+1}) - x(t^{n+1})$ are $\mathrm{O}(\Delta t^2)$ if the conditions (25b), (25c), (25e)–(25g) and (25i) are satisfied, and therefore $\Psi_i = \mathrm{O}(\Delta t^3)$, which proves that the ALE scheme (9) is second-order time-accurate on moving grids. □

It is interesting to note that: (a) both Propositions 1 and 2 lead to similar if not identical conditions on the parameterization (11a)–(11c), and (b) these conditions decouple the parameters associated with the discretization of the convective fluxes from those associated with the discretization of the diffusive fluxes and source terms.

5. Examples

Here, we consider six different extensions to moving grids of the three-point backward difference scheme. The first two (schemes A and B) preserve its second-order time-accuracy, while the last four (schemes C–F) destroy it. Schemes C and D do so by choosing values for the parameters α, ζ and θ associated with the discretization of the convective fluxes which violate some of the conditions (12a)–(12f) or (25a)–(25f). Schemes E and F loose the second-order time-accuracy of their fixed grid counterpart by choosing values for the parameters β and η associated with the discretization of the diffusive fluxes and source terms which violate some of the conditions (12g)–(12i) or (25g)–(25i).

5.1. ALE extensions preserving the second-order time-accuracy

5.1.1. Scheme A

The restriction to the Euler equations of scheme A presented here was first derived in [9] without paying formal attention to time-accuracy. It is compatible with both frameworks (8) and (9). It uses four mesh configurations for discretizing the convective fluxes, and the mesh configuration at t^{n+1} for discretizing the diffusive fluxes and source terms. It is defined by

$$\zeta_1^{n+1} = \frac{1}{2}\left(1 + \frac{1}{\sqrt{3}}\right), \quad \zeta_1^{n} = \frac{1}{2}\left(1 - \frac{1}{\sqrt{3}}\right), \quad \zeta_1^{n-1} = 0, \tag{36}$$

$$\zeta_2^{n+1} = \frac{1}{2}\left(1 - \frac{1}{\sqrt{3}}\right), \quad \zeta_2^{n} = \frac{1}{2}\left(1 + \frac{1}{\sqrt{3}}\right), \quad \zeta_2^{n-1} = 0, \tag{37}$$

$$\zeta_3^{n+1} = 0, \quad \zeta_3^n = \frac{1}{2}\left(1 + \frac{1}{\sqrt{3}}\right), \quad \zeta_3^{n-1} = \frac{1}{2}\left(1 - \frac{1}{\sqrt{3}}\right), \tag{38}$$

$$\zeta_4^{n+1} = 0, \quad \zeta_4^n = \frac{1}{2}\left(1 - \frac{1}{\sqrt{3}}\right), \quad \zeta_4^{n-1} = \frac{1}{2}\left(1 + \frac{1}{\sqrt{3}}\right), \tag{39}$$

$$\theta_1^{n+1} = \theta_2^{n+1} = 1, \quad \theta_1^n = \theta_2^n = -1, \quad \theta_1^{n-1} = \theta_2^{n-1} = 0, \tag{40}$$

$$\theta_3^{n+1} = \theta_4^{n+1} = 0, \quad \theta_3^n = \theta_4^n = 1, \quad \theta_3^{n-1} = \theta_4^{n-1} = -1, \tag{41}$$

$$\eta_1^{n+1} = 1, \quad \eta_1^n = 0, \quad \eta_1^{n-1} = 0, \tag{42}$$

and

$$\alpha_1 = \alpha_2 = \frac{3}{4}, \quad \alpha_3 = \alpha_4 = -\frac{1}{4}, \quad \beta_1 = 1. \tag{43}$$

The above parameters satisfying the conditions (12a)–(12i) and (25a)–(25i), scheme A presented here is formally second-order time-accurate on moving grids. In [9], it is shown that this scheme satisfies its DGCL. We also note that the two-dimensional version of this scheme was first derived in [3].

5.1.2. Scheme B

Scheme B presented here is also compatible with both frameworks (8) and (9). It employs only the mesh configuration at t^{n+1}, and therefore is much simpler than scheme A. It is defined by

$$\zeta_1^{n+1} = 1, \quad \zeta_1^n = 0, \quad \zeta_1^{n-1} = 0, \tag{44}$$

$$\theta_1^{n+1} = \frac{3}{2}, \quad \theta_1^n = -2, \quad \theta_1^{n-1} = \frac{1}{2}, \tag{45}$$

$$\eta_1^{n+1} = 1, \quad \eta_1^n = 0, \quad \eta_1^{n-1} = 0, \tag{46}$$

and

$$\alpha_1 = \beta_1 = 1. \tag{47}$$

The above parameters satisfying the conditions (12a)–(12i) and (25a)–(25i), scheme B specified here is formally second-order time-accurate on moving meshes. However, from the results proved in [9], it follows that this scheme does not satisfy its DGCL. Hence, satisfying its DGCL is not a necessary condition for an ALE scheme to preserve the order of time-accuracy of its fixed grid counterpart.

5.2. ALE extensions loosing the second-order time-accuracy

5.2.1. Scheme C

Scheme C specified here uses the framework defined by Eq. (9) except for the computation of the normal velocity (see Appendix A). It is based on one mesh configuration at t^n for the discretization of the convective fluxes, and one mesh configuration at t^{n+1} for discretization of the diffusive and source terms. It is defined by

$$\zeta_1^{n+1} = 0, \quad \zeta_1^n = 1, \quad \zeta_1^{n-1} = 0, \tag{48}$$

$$\eta_1^{n+1} = 1, \quad \eta_1^n = 0, \quad \eta_1^{n-1} = 0, \tag{49}$$

and

$$\alpha_1 = \beta_1 = 1. \tag{50}$$

In Appendix A, we show that this scheme is formally first-order time-accurate on moving meshes and satisfies its DGCL. This result is compatible with the theoretical result established in [6] given that a first-order time-accurate scheme is a consistent scheme. More importantly, scheme C shows that satisfying its DGCL is not a sufficient condition for preserving the order of time-accuracy.

5.2.2. Scheme D

The scheme presented here is compatible with both frameworks (8) and (9). It employs the mesh configuration at t^n for discretizing the convective fluxes, and the mesh configuration at t^{n+1} for discretizing the diffusive fluxes and source terms. Its parameters are given by

$$\zeta_1^{n+1} = 0, \quad \zeta_1^n = 1, \quad \zeta_1^{n-1} = 0, \tag{51}$$

$$\theta_1^{n+1} = 1, \quad \theta_1^n = -1, \quad \theta_1^{n-1} = 0, \tag{52}$$

$$\eta_1^{n+1} = 1, \quad \eta_1^n = 0, \quad \eta_1^{n-1} = 0, \tag{53}$$

and

$$\alpha_1 = \beta_1 = 1. \tag{54}$$

The above parameters do not satisfy conditions (12e), (12f), (25e) and (25f). Hence, scheme D is not second-order time-accurate on moving meshes. It is only first-order time-accurate and according to [9] it does not satisfy its DGCL.

5.2.3. Scheme E

Scheme E specified below uses the same discretization as scheme A for the convective fluxes, but evaluates the diffusive fluxes and source terms on the mesh configuration at $t^{n+1/2}$ [10]. Its parameters are given by

$$\eta_1^{n+1} = \frac{1}{2}, \quad \eta_1^n = \frac{1}{2}, \quad \eta_1^{n-1} = 0, \tag{55}$$

and

$$\beta_1 = 1. \tag{56}$$

The above parameters do not satisfy conditions (12i) and (25i). This scheme is formally first-order time-accurate on moving meshes. It satisfies its DGCL [9].

5.2.4. Scheme F

Scheme F described here uses the same discretization as scheme A for the convective fluxes, but evaluates the diffusive fluxes and source terms on the mesh configuration at t^n. It is defined by

$$\eta_1^{n+1} = 0, \quad \eta_1^n = 1, \quad \eta_1^{n-1} = 0, \tag{57}$$

and

$$\beta_1 = 1. \tag{58}$$

The above parameters do not satisfy conditions (12i) and (25i). Scheme F presented here is formally first-order time-accurate on moving grids. From the conditions given in [9], it follows that this scheme satisfies its DGCL.

6. Applications

In order to illustrate the theoretical results presented in this paper, we consider here the solution of inviscid as well as viscous, unsteady, nonlinear flow problems associated with the AGARD Wing 445.6, and a complete F-16 configuration. To this effect, we use the AERO-F flow solver developed at the University of Colorado with aeroelastic applications in mind [11,12].

AERO-F is a domain decomposition based parallel three-dimensional Euler and Navier–Stokes solver which features a combination of finite volume and finite element discretizations on unstructured tetrahedral meshes. It blends an upwind scheme for the convective fluxes based on Roe's approximate Riemann solver [13] and a piecewise linear reconstruction of the flow variables in each control volume [14,15], with a P1 finite element Galerkin approximation of the diffusive fluxes and source terms [16,17,10]. It performs turbulence modeling by solving the one-equation Spalart–Allmaras model [18] and coupling it with Reichardt's wall function [19] and Spalding's wall boundary condition [20] for the eddy viscosity. Because the governing equation for this turbulence model is similar to the averaged Navier–Stokes equations, it is discretized in the same manner except for the use of a constant reconstruction in order to ensure the positivity of the turbulence variable.

In principle, AERO-F is equipped with the ALE version of the three-point backward difference scheme summarized in Section 5.1.1 (scheme A). However, for this study we have equipped AERO-F with all ALE time-integrators presented in Section 5 (schemes B–F). Since these schemes are implicit, AERO-F must solve at each time-step a system of nonlinear equations. For this purpose, it relies on various Newton-like methods. A secondary objective of this paper is to highlight the effect of a certain usage of such methods on the time-accuracy of a flow solver. One such Newton-like method uses a defect–correction procedure [21] in which the Jacobian matrix is obtained from the linearization of a first-order approximation method, and the right-hand side is approximated by a second-order method. This approach results in a well-conditioned Jacobian matrix, and is characterized by a lower storage requirement than the Jacobian matrix obtained from the linearization of a second-order approximation method. However, as most inexact Newton methods, it does not deliver a quadratic convergence rate. Another inexact Newton method employed by AERO-F is based on a finite difference Newton–Krylov method [22–24]. This method is computationally more expensive than that based on the defect–correction procedure but delivers a better convergence rate and requires less memory. In all cases, AERO-F relies on the GMRES [25] method preconditioned by the RAS [26] algorithm for solving iteratively the large sparse linear systems of equations that arise at each Newton-like iteration.

6.1. Forced oscillations of the AGARD Wing 445.6

Here, we consider the simulation of forced oscillations of the AGARD Wing 445.6 [27]. This wing is an AGARD standard aeroelastic configuration with a 45° quarter-chord sweep angle, a panel aspect ratio of 1.65, a taper ratio of 0.66, and a NACA 65A004 airfoil section. We clamp it at its root and force it to vibrate according to

$$x = x_0 + (x_b - x_0)\sin(2\pi f t), \tag{59}$$

where x_0 and x_b denote the undeformed position and a position associated with the first bending mode of this wing (see Fig. 1(a)), respectively, and f denotes here the vibration frequency that is set to 14.92 Hz.

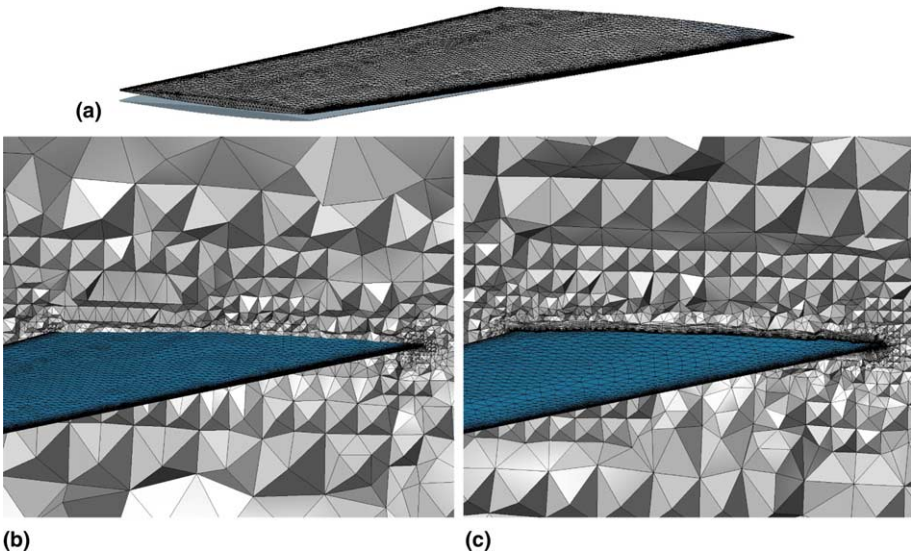

Fig. 1. AGARD Wing 445.6: (a) undeformed (solid) and deformed (solid and wireframe) shapes; (b) isotropic mesh (178,938 nodes); (c) anisotropic mesh (426,697 nodes).

We set the freestream conditions to $M = 0.5$, $\alpha = 2°$, $\beta = 0°$, $\rho = 1.117 \times 10^{-7}$ slugs $\times$ ft/in.^{4}, and $p = 11$ psi.

To begin, we assume that the flow is inviscid and generate a three-dimensional tetrahedral mesh with 178,938 nodes (see Fig. 1(b)). First, we perform one simulation using scheme A and an extremely small time-step ($\Delta t = 0.00001$ s) in order to generate a reference solution in lieu of an "exact" solution until $t = 0.1$ s. Then, we compute various solutions of this forced oscillations problem using schemes A–D and a suite of time-steps varying between $\Delta t = 0.001$ and $\Delta t = 0.01$ s. In all cases, we perform at each time-step a sufficiently large number of Newton-like iterations to ensure that the nonlinear system of equations is properly solved. We report in Fig. 2(a) the measured errors as a function of the time-step in log–log format. The error is defined as the L2 norm of the vector collecting for all the conservative flow

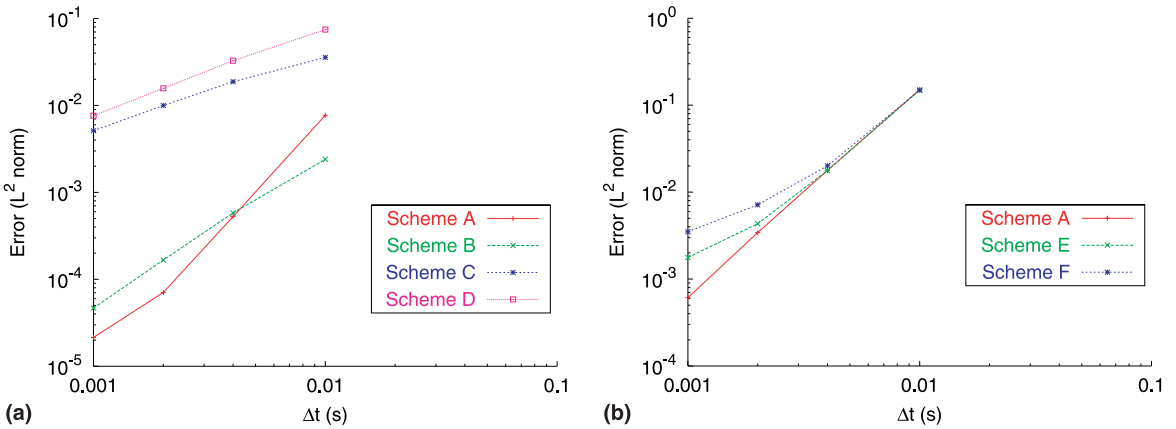

Fig. 2. Accuracy analysis for forced oscillations of the AGARD Wing 445.6: (a) inviscid flow case; (b) viscous flow case.

variables and all the grid points the difference between the numerical and reference solutions. The error associated with scheme A, which is provably second-order time-accurate on moving grids and satisfies its DGCL, exhibits a slope equal to 2.55. For scheme B which is also provably second-order time-accurate on moving grids but violates its DGCL, the slope of the error curve is equal to 1.83. For schemes C and D which are provably first-order time-accurate on moving grids, the slope of the error curve is, respectively, 0.96 and 1.05. Hence, all these numerical results are in good agreement with the theoretical results presented in this paper.

To highlight the influence of a specific usage of an inexact Newton method on the delivered time-accuracy, we report in Fig. 3 the effect of this usage on the error associated with scheme A. The reader can observe that when the defect–correction procedure is used (see Fig. 3(a)), more than five Newton iterations are required for scheme A to achieve a second-order time-accuracy. On the other hand, when scheme A is equipped with the finite difference Krylov approach, only one Newton-like iteration is needed to achieve a second-order time-accuracy (see Fig. 3(b)). From this observation and the CPU results summarized in Table 1, one can conclude that the finite difference Krylov approach is more effective than the defect–correction procedure. For this reason, all simulations discussed in the remainder of this section have been performed with two finite difference Newton–Krylov iterations per time-step.

Next, we model the flow by the averaged Navier–Stokes equations supplemented by the Spalart–Allmaras turbulence model, and set the Reynolds number based on the mean chord to 5×10^6. For this purpose, we generate a three-dimensional tetrahedral mesh with 426,697 nodes (see Fig. 1(c)). Following the same procedure as in the inviscid case, we report in Fig. 2(b) the variation with the time-step of the error obtained for schemes A, E and F. The reader can observe that only scheme A in which the viscous fluxes

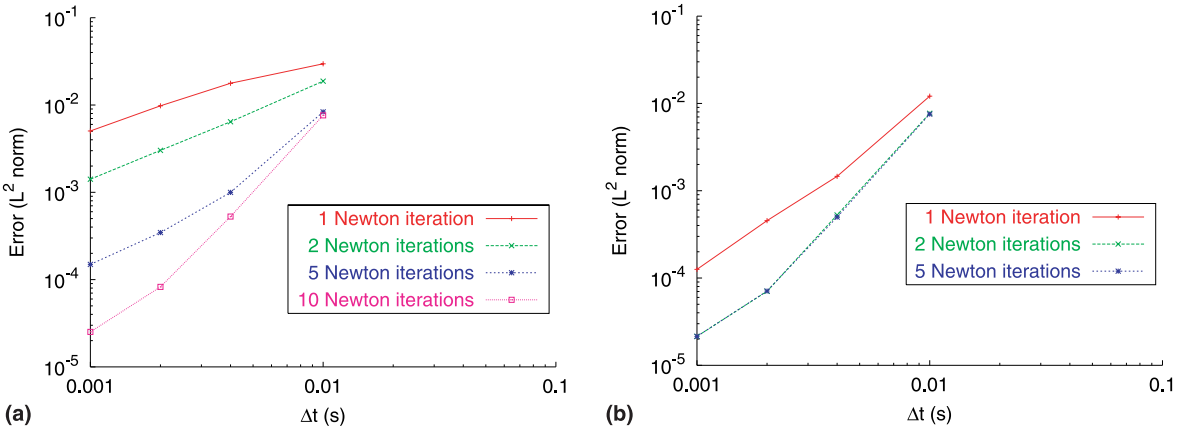

Fig. 3. Accuracy analysis for forced oscillations of the AGARD Wing 445.6: (a) defect–correction approach; (b) finite difference Krylov approach.

Table 1
Forced oscillations AGARD Wing 445.6 – CPU time (in seconds) for 100 time-steps on 16 processors SGI Origin 3200

Number of Newton iterations	1	2	5	10
Defect–correction approach	454	795	1744	3225
Finite difference Krylov approach	1024	1814	5339	–

and source terms are computed at each time-step on the latest mesh configuration delivers a second-order time-accuracy, which is in agreement with Proposition 2.

6.2. Aeroelastic response of the AGARD Wing 445.6

Here, we consider the simulation of an aeroelastic response of the AGARD Wing 445.6. The structural model selected here is the so-called 2.5-ft weakened model 3 whose measured modal frequencies and wind-tunnel flutter test results are reported in [27], and for which computational aeroelastic data can be found in [28,29]. We construct an undamped finite element structural model of this wing with 800 triangular composite shell elements and 2646 degrees of freedom using the information given in [27]. This model yields natural mode shapes and frequencies that are similar to those derived experimentally. We also construct a three-dimensional tetrahedral fluid mesh that contains 178,938 nodes (see Fig. 1(b)). We assume that the flow is inviscid and set the freestream conditions to $M = 0.901$, $\rho = 1.117 \times 10^{-7}$ slugs $\times$ ft/in.^{4} and $p = 11$ psi. We perturb the finite element structural model along its first bending mode, and compute a steady-state solution around the deformed configuration of the wing. Next, we use this perturbation as an initial condition, and compute the aeroelastic response of the wing by a partitioned procedure for the solution of fluid–structure interaction problems [2]. In this partitioned procedure, the mid-point rule is used to time-integrate the semi-discrete equations of dynamic equilibrium of the structural model while the flow field is advanced in time using different extensions on moving grids of the three-point backward difference scheme.

We perform four computations with schemes A–D and a fluid–structure coupling time-step $\Delta t = 0.001$ s. This time-step corresponds to sampling the period of the first torsional mode of the dry wing in 25 points, as usually done for any second-order implicit time-integration scheme. Fig. 4 reports the computed aeroelastic responses and compares them with a reference solution obtained with a time-step $\Delta t = 0.0001$ s. The response obtained by the methods preserving the second-order time-accuracy match nicely the reference curve and predict that for the given freestream conditions the AGARD Wing 445.6 will not flutter. This is consistent with the experimental data published in [27] and the computational results are presented in [28,29]. For the same dimensional coupling time-step, the methods that are only first-order time-accurate predict erroneously flutter. These results highlight the significance of the mathematical results presented in this paper on practical fluid–structure applications.

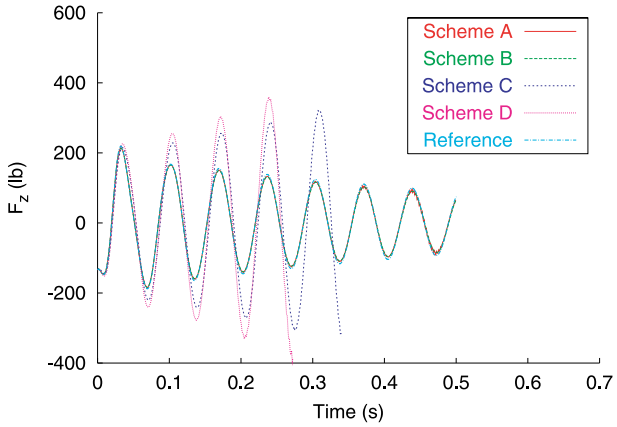

Fig. 4. Vertical force history for the aeroelastic response of the AGARD Wing 445.6 (the curves associated with schemes A and B are superimposed with the reference curve).

6.3. Forced oscillations of an F-16 fighter

As a second example for illustrating the impact on industrial applications of the developments presented in this paper, we simulate the response to forced oscillations of an F-16 fighter configuration in the transonic regime. We set the freestream conditions to $M = 0.9$, $\alpha = 2°$, $\beta = 0°$, $\rho = 8.44 \times 10^{-8}$ slugs $\times$ ft/in.^{4} and $p = 10.11$ psi, and force the fighter to vibrate according to Eq. (59) where the deformed configuration is taken as twice the static aeroelastic deformation at the same altitude of 10,000 ft (see Fig. 5) and the frequency of the oscillations is set to 7 Hz. The three-dimensional tetrahedral mesh used for this inviscid flow simulation contains 403,919 grid points.

Fig. 6 compares the measured errors of schemes A–D as a function of the time-step in log–log format. Schemes A and B, which are provably second-order time-accurate on moving grids, exhibit error slopes equal to 1.99 and 2.01, respectively. The error slopes associated with schemes C and D, which are provably first-order time-accurate on moving grids, are equal to 1.03 and 1.04, respectively. Hence, these results confirm the applicability of the theoretical results proved in this paper.

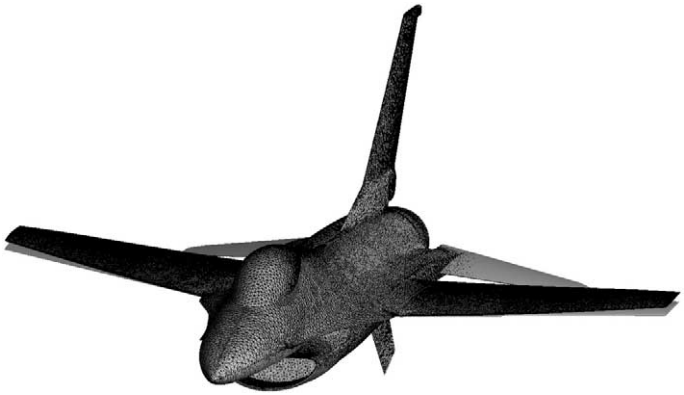

Fig. 5. Undeformed (solid) and deformed (solid and wireframe) configurations for an F-16 fighter.

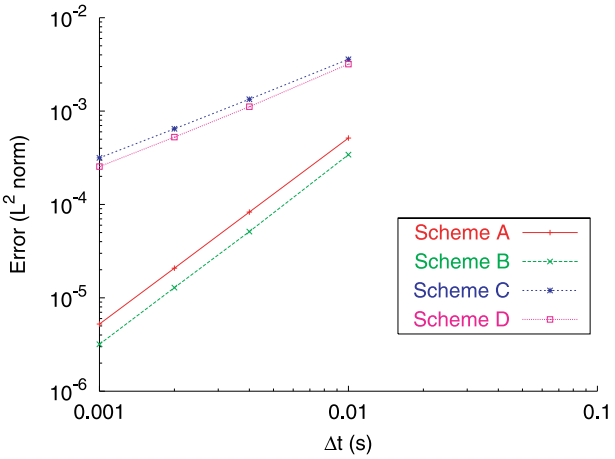

Fig. 6. Accuracy analysis for forced oscillations of an F-16 fighter.

7. Conclusions

Most often, an ALE time-integrator is typically constructed by combining a preferred time-integrator for fixed grids computations and an ad hoc procedure for evaluating the geometric quantities arising from the ALE formulation. Such an approach for designing an ALE time-discretization is simple, but does not necessarily preserve the order of time-accuracy of the underlying basic time-integrator. To address this issue, we have presented two different methods for extending to moving grids a preferred time-integrator while preserving its order of time-accuracy established on fixed grids. These methods differ in the approaches they adopt for time-integrating between time t^n and time t^{n+1} the convective, diffusive and source terms, when the grid moves from a position x^n to a position x^{n+1}. For each time-interval $[t^n, t^{n+1}]$, the first method evaluates the numerical fluxes and source terms on a sequence of intermediate mesh configurations, then time-averages each set of these numerical quantities. The second method constructs a single computational mesh configuration in the time-interval $[t^n, t^{n+1}]$ by time-averaging a set of intermediate mesh configurations, then computes the numerical fluxes and source terms on this time-averaged mesh configuration. In both methods, the geometric quantities arising from the ALE formulation, the parameters governing the construction of the intermediate mesh configurations and the time-averaging procedure are chosen as to guarantee that the resulting ALE time-integrator is formally p-order time-accurate on moving grids, where p characterizes the underlying fixed grid time-integrator. Each of these two approaches can lead to multiple ALE versions of a basic scheme that preserve its order of time-accuracy on moving grids. However, not all of these versions satisfy their discrete geometric conservation laws (DGCL), which shows that the DGCL is not a necessary condition for an ALE numerical scheme to preserve on moving grids its order of time-accuracy established on fixed grids. We have also shown that for this purpose, the DGCL is neither a sufficient condition. Using sample inviscid as well as viscous, unsteady, nonlinear flow problems associated with the AGARD Wing 445.6 and a complete F-16 configuration, we have highlighted the importance of preserving a given order of time-accuracy on moving grids, particularly when solving aeroelastic problems in the time domain.

Acknowledgements

The first and last author acknowledge the support by the Air Force Office of Scientific Research under Grant F49620-01-1-0129. They thank Kristoffer G. van der Zee at TU Delft for his numerous suggestions that have improved this paper. They also thank ICEM CFD Engineering Inc. for providing their mesh generation software.

Appendix A. First-order time-accurate extension to moving grids of the three-point backward difference scheme that satisfies its DGCL

The objective of this section is to show that scheme C presented in Section 5.2.1 is first-order time-accurate on moving grids and satisfies its DGCL. Because viscous fluxes do not affect the DGCL [9], we focus on the inviscid version of scheme C and prove both stated results. Following the same approach presented here, the reader can easily show that the viscous version of scheme C is also first-order time-accurate on moving grids.

When a finite volume discretization is applied to the ALE conservative form of the Euler equations

$$\left.\frac{\partial Ju}{\partial t}\right|_{\xi} + J\nabla_x \cdot (F(u) - wu) = 0, \tag{A.1}$$

the integration over a reference cell $\Omega_i(0)$ in the ξ space leads to

$$\frac{\mathrm{d}}{\mathrm{d}t}\int_{\Omega_i(0)} uJ \,\mathrm{d}\Omega_\xi + \int_{\Omega_i(0)} \nabla_x \cdot (F(u) - wu)J \,\mathrm{d}\Omega_\xi = 0, \tag{A.2}$$

which, in view of Eqs. (1) and (2), can be transformed into

$$\frac{\mathrm{d}}{\mathrm{d}t}\int_{\Omega_i(t)} u \,\mathrm{d}\Omega_x + \int_{\Omega_i(t)} \nabla_x \cdot (F(u) - wu) \,\mathrm{d}\Omega_x = 0. \tag{A.3}$$

Integrating by part the second term in the above equation gives

$$\frac{\mathrm{d}}{\mathrm{d}t}\int_{\Omega_i(t)} u \,\mathrm{d}\Omega_x + \int_{\partial\Omega_i(t)} (F(u) - wu) \cdot \mu \,\mathrm{d}s = 0, \tag{A.4}$$

where μ denotes the unitary normal to the cell boundary $\partial\Omega_i$. Let $V(i)$ denote the set of vertices connected to vertex i, and for each $j \in V(i)$, let $\partial\Omega_{ij} = \partial\Omega_i \cap \partial\Omega_j$. The second term in Eq. (A.4) can be evaluated on an interface-by-interface basis as follows:

$$\int_{\partial\Omega_i(t)} (F(u) - wu) \cdot \mu \,\mathrm{d}s = \sum_{j\in V(i)} \int_{\partial\Omega_{ij}(t)} (F(u) - wu) \cdot \mu_{ij} \,\mathrm{d}s, \tag{A.5}$$

where μ_{ij} is the unitary normal to $\partial\Omega_{ij}$. Typically, each term in the above sum is approximated by a numerical flux function Φ – for example, using an (approximate) Riemann solver [13] – in the following manner:

$$\int_{\partial\Omega_{ij}(t)} (F(u) - wu) \cdot \mu_{ij} \,\mathrm{d}s \approx \Phi(u_i, u_j, v_{ij}, \kappa_{ij}), \tag{A.6}$$

where the non-unitary normal and normal velocity to the cell boundary $\partial\Omega_{ij}$ are given by

$$v_{ij} = \int_{\partial\Omega_{ij}(t)} \mu_{ij} \,\mathrm{d}s, \tag{A.7}$$

$$\kappa_{ij} = \int_{\partial\Omega_{ij}(t)} w \cdot \mu_{ij} \,\mathrm{d}s. \tag{A.8}$$

Finally, substituting Eq. (A.6) into Eq. (A.4) and time-integrating Eq. (A.4) with the three-point backward difference scheme gives

$$\frac{3}{2}(\Omega u)_i^{n+1} - 2(\Omega u)_i^n + \frac{1}{2}(\Omega u)_i^{n-1} + \Delta t \sum_{j\in V(i)} \Phi(u_i^{n+1}, u_j^{n+1}, \bar{v}_{ij}, \bar{\kappa}_{ij}) = 0, \tag{A.9}$$

where $\bar{v}_{ij}$ and $\bar{\kappa}_{ij}$ denote the respective discrete values of v_{ij} and κ_{ij} that need to be determined in order to complete the description of the above scheme.

The DGCL associated with the above scheme is obtained by assuming a constant solution $u = u^* \neq 0$. Hence, Eq. (A.9) becomes

$$\frac{3}{2}\Omega_i^{n+1}u^* - 2\Omega_i^n u^* + \frac{1}{2}\Omega_i^{n-1}u^* + \Delta t \sum_{j\in V(i)} \Phi(u^*, u^*, \bar{v}_{ij}, \bar{\kappa}_{ij}) = 0. \tag{A.10}$$

In general, the numerical flux is required to be consistent so that

$$\Phi(u^*, u^*, \bar{v}_{ij}, \bar{\kappa}_{ij}) = F(u^*) \cdot \bar{v}_{ij} - \bar{\kappa}_{ij}u^*. \tag{A.11}$$

This transforms Eq. (A.10) into

$$u^*\left(\frac{3}{2}\Omega_i^{n+1} - 2\Omega_i^n + \frac{1}{2}\Omega_i^{n-1} - \Delta t \sum_{j\in V(i)} \bar{\kappa}_{ij}\right) + \Delta t F(u^*)\cdot \sum_{j\in V(i)} \bar{v}_{ij} = 0. \tag{A.12}$$

However,

$$\sum_{j\in V(i)} \bar{v}_{ij} = 0 \tag{A.13}$$

because the cells are required to remain closed during the mesh motion. Hence, Eq. (A.12) becomes

$$\frac{3}{2}\Omega_i^{n+1} - 2\Omega_i^n + \frac{1}{2}\Omega_i^{n-1} = \Delta t \sum_{j\in V(i)} \bar{\kappa}_{ij} \tag{A.14}$$

which is the DGCL associated with scheme (A.9). The above equation can also be rewritten as

$$\frac{3}{2}\Delta\Omega_i^{n+1} - \frac{1}{2}\Delta\Omega_i^n = \Delta t \sum_{j\in V(i)} \bar{\kappa}_{ij}, \tag{A.15}$$

where

$$\Delta\Omega_i^{n+1} = \Omega_i^{n+1} - \Omega_i^n = \sum_{j\in V(i)} \Delta\Omega_{ij}^{n+1} \tag{A.16}$$

and

$$\Delta\Omega_{ij}^{n+1} = \int_{t^n}^{t^{n+1}} \int_{\partial\Omega_{ij}(t)} w\cdot\mu_{ij}\,\mathrm{d}s\,\mathrm{d}t \tag{A.17}$$

is the volume swept by the part of the control volume interface between nodes i and j during the time-interval $[t^n, t^{n+1}]$. This term can be computed by the formula given in [5,30]. Therefore, Eq. (A.15) becomes

$$\frac{3}{2}\sum_{j\in V(i)} \Delta\Omega_{ij}^{n+1} - \frac{1}{2}\sum_{j\in V(i)} \Delta\Omega_{ij}^n = \Delta t \sum_{j\in V(i)} \bar{\kappa}_{ij} \tag{A.18}$$

and thus computing the normal velocity as

$$\bar{\kappa}_{ij} = \frac{\frac{3}{2}\Delta\Omega_{ij}^{n+1} - \frac{1}{2}\Delta\Omega_{ij}^n}{\Delta t} \tag{A.19}$$

guarantees that scheme (A.9) satisfies its DGCL regardless of how $\bar{v}_{ij}$ is evaluated.

Now, following the same argument as in Section 4, the local truncation error of the ALE scheme (A.9) is

$$\begin{aligned}\Psi_i = {} & \Delta t \sum_{j\in V(i)} \nabla_{v_{ij}} \Phi(u_i(t^{n+1}), u_j(t^{n+1}), v_{ij}(t^{n+1}), \kappa_{ij}(t^{n+1}))(\bar{v}_{ij}(t^{n+1}) - v_{ij}(t^{n+1})) \\ & + \Delta t \sum_{j\in V(i)} \nabla_{\kappa_{ij}} \Phi(u_i(t^{n+1}), u_j(t^{n+1}), v_{ij}(t^{n+1}), \kappa_{ij}(t^{n+1}))(\bar{\kappa}_{ij}(t^{n+1}) - \kappa_{ij}(t^{n+1})) \\ & + \Delta t \sum_{j\in V(i)} \mathrm{O}(\|\bar{v}_{ij}(t^{n+1}) - v_{ij}(t^{n+1})\|^2 + \|\bar{\kappa}_{ij}(t^{n+1}) - \kappa_{ij}(t^{n+1})\|^2) + \mathrm{O}(\Delta t^3).\end{aligned} \tag{A.20}$$

From Eqs. (A.17) and (A.8), it follows that

$$\Delta\Omega_{ij}^{n+1} = \int_{t^n}^{t^{n+1}} \kappa_{ij}\,\mathrm{d}t = \int_{t^n}^{t^{n+1}} \left(\kappa_{ij}(t^{n+1}) + \frac{\mathrm{d}\kappa_{ij}}{\mathrm{d}t}(t^{n+1})(t-t^{n+1}) + \mathrm{O}(\Delta t^2)\right)\mathrm{d}t$$
$$= \kappa_{ij}(t^{n+1})\Delta t - \frac{1}{2}\frac{\mathrm{d}\kappa_{ij}}{\mathrm{d}t}(t^{n+1})\Delta t^2 + \mathrm{O}(\Delta t^3) \tag{A.21}$$

and a similar argument applied to $\Delta\Omega_{ij}^{n}$ gives

$$\Delta\Omega_{ij}^{n} = \kappa_{ij}(t^{n+1})\Delta t - \frac{3}{2}\frac{\mathrm{d}\kappa_{ij}}{\mathrm{d}t}(t^{n+1})\Delta t^2 + \mathrm{O}(\Delta t^3). \tag{A.22}$$

Hence, from Eqs. (A.19), (A.21) and (A.22), the quantity $\bar{\kappa}_{ij} - \kappa_{ij}(t^{n+1})$ is $\mathrm{O}(\Delta t^2)$. From Eqs. (32) and (21), it follows that the quantity $\bar{v}_{ij}(t^{n+1}) - v_{ij}(t^{n+1})$ is $\mathrm{O}(\Delta t)$ if $\bar{v}_{ij} = v_{ij}^n$, and therefore $\Psi_i = \mathrm{O}(\Delta t^2)$ which proves that the ALE scheme (A.9) with this choice of parameters $\bar{v}_{ij}$ and $\bar{\kappa}_{ij}$ is only first-order time-accurate on moving grids.

Remark. We note however that a second-order time-accurate version of scheme (A.9) can be constructed. Choosing $\bar{v}_{ij} = v_{ij}^{n+1}$ makes the quantity $\bar{v}_{ij}(t^{n+1}) - v_{ij}(t^{n+1})$ become $\mathrm{O}(\Delta t^2)$. Consequently, the local truncation error is $\mathrm{O}(\Delta t^3)$ which proves that this version of the ALE scheme (A.9) is second-order accurate on moving grids.

References

[1] J. Donea, An arbitrary Lagrangian–Eulerian finite element method for transient fluid–structure interactions, Computer Methods in Applied Mechanics and Engineering 33 (1982) 689–723.
[2] C. Farhat, M. Lesoinne, N. Maman, Mixed explicit/implicit time integration of coupled aeroelastic problems: three-field formulation, geometric conservation and distributed solution, International Journal for Numerical Methods in Fluids 21 (1995) 807–835.
[3] A. Løvli, A.H. Strømmen, Order of time integration schemes on dynamic meshes, Technical Report Preprint Numerics No. 8/2001, Norwegian University of Science and Technology, Trondheim, Norway, 2001.
[4] F. Nobile, Numerical approximation of fluid–structure interaction problems with application to hemodynamics, Ph.D. Thesis, École Polytechnique Fédérale de Lausanne, Switzerland, September, 2001.
[5] M. Lesoinne, C. Farhat, Geometric conservation laws for flow problems with moving boundaries and deformable meshes and their impact on aeroelastic computations, Computer Methods in Applied Mechanics and Engineering 134 (1996) 71–90.
[6] H. Guillard, C. Farhat, On the significance of the geometric conservation law for flow computations on moving meshes, Computer Methods in Applied Mechanics and Engineering 190 (2000) 1467–1482.
[7] C. Farhat, P. Geuzaine, C. Grandmont, The discrete geometric conservation law and the nonlinear stability of ALE schemes for the solution of flow problems on moving grids, Journal of Computational Physics 174 (2001) 669–694.
[8] C. Farhat, P. Geuzaine, C. Grandmont, The discrete geometric conservation law and its effects on nonlinear stability and accuracy, AIAA paper 2001-2607, June, 2001.
[9] B. Koobus, C. Farhat, Second-order time-accurate and geometrically conservative implicit schemes for flow computations on unstructured dynamic meshes, Computer Methods in Applied Mechanics and Engineering 170 (1999) 103–130.
[10] B. Koobus, C. Farhat, On the implicit time integration of semi-discrete viscous fluxes on unstructured dynamic meshes, International Journal for Numerical Methods in Fluids 29 (1999) 975–996.
[11] C. Farhat, P. Geuzaine, G. Brown, Application of a three-field nonlinear fluid–structure formulation to the prediction of the aeroelastic parameters of an F-16 fighter, Computers and Fluids 32 (1) (2003) 3–29.
[12] P. Geuzaine, G. Brown, C. Harris, C. Farhat, Aeroelastic dynamic analysis of a full F-16 configuration for various flight conditions, AIAA Journal 41 (3) (2003) 363–371.
[13] P.L. Roe, Approximate Riemann solvers, parameter vectors and difference schemes, Journal of Computational Physics 43 (1981) 357–372.
[14] B. van Leer, Towards the ultimate conservative difference scheme. V. A second-order sequel to Godunov's method, Journal of Computational Physics 32 (1979) 101–136.

[15] A. Dervieux, Steady Euler simulations using unstructured meshes, in: Proceedings of the VKI Lectures Series 1985-04, 16th Computational Fluid Dynamics, von Karman Institute, Brussels, Belgium, 1985.
[16] F. Fezoui, S. Lanteri, B. Larrouturou, C. Olivier, Résolution numérique des équations de Navier–Stokes pour un fluide compressible en maillage triangulaire, Technical Report 1033, INRIA, France, 1989.
[17] T.J. Barth, Numerical aspects of computing high Reynolds number flows on unstructured meshes, AIAA paper 91-0721, January, 1991.
[18] P.R. Spalart, S.R. Allmaras, A one-equation turbulence model for aerodynamic flows, AIAA paper 92-0439, January, 1992.
[19] H. Reichardt, Vollständige Darstellung der turbulenten Geschwindigkeitsverteilung in glatten Leitungen, Zeitschrift für Angewandte Mathematik und Mechanik 31 (1951) 208–219.
[20] F.M. White, Viscous Fluid Flow, McGraw-Hill, New York, 1974.
[21] K. Böhmer, P.W. Hemker, H.J. Stetter, The defect correction approach, in: K. Böhmer, H.J. Stetter (Eds.), Defect Correction Methods: Theory and Applications, Computing Supplementa, vol. 5, Springer, Berlin, 1984, pp. 1–32.
[22] P.N. Brown, Y. Saad, Hybrid Krylov methods for nonlinear systems of equations, SIAM Journal on Scientific and Statistical Computing 11 (3) (1990) 450–481.
[23] D.E. Keyes, V. Venkatakrishnan, Newton–Krylov–Schwarz methods: interfacing sparse linear solvers with nonlinear applications, Zeitschrift für Angewandte Mathematik und Mechanik 76 (1996) 147–150.
[24] P. Geuzaine, Newton–Krylov strategy for compressible turbulent flows on unstructured meshes, AIAA Journal 39 (3) (2001) 528–531.
[25] Y. Saad, M.H. Schultz, GMRES: a generalized minimal residual algorithm for solving nonsymmetric linear problems, SIAM Journal on Scientific and Statistical Computing 7 (3) (1986) 856–869.
[26] X.C. Cai, C. Farhat, M. Sarkis, A minimum overlap restricted additive Schwarz preconditioner and applications in 3D flow simulations, Contemporary Mathematics 218 (1998) 478–484.
[27] E.C. Yates, AGARD standard aeroelastic configuration for dynamic response, candidate configuration I. – Wing 445.6, Technical Report TM-100492, NASA, 1987.
[28] E.M. Lee-Rausch, J.T. Batina, Wing-flutter boundary prediction using unsteady Euler aerodynamic method, AIAA paper 93-1422, April, 1993.
[29] K.K. Gupta, Development of a finite element aeroelastic analysis capability, Journal of Aircraft 33 (5) (1996) 995–1002.
[30] B. Nkonga, H. Guillard, Godunov type method on non-structured meshes for three-dimensional moving boundary problems, Computer Methods in Applied Mechanics and Engineering 113 (1994) 183–204.